RSC Advances

ROYAL SOCIETY OF CHEMISTRY

www.rsc.org/advances

Journal Name

ARTICLE TYPE

Hierarchical porous CuO nanostructures with tunable properties for high performance supercapacitors

Yang Lu,[a,b,c] Hailong Yan,[a,b] Kangwen Qiu,[a,b] Jinbing Cheng,[a,b] Weixiao Wang,[a,b] Xianming Liu,[d] Chengchun Tang,[c*] Jang-Kyo Kim[e] and Yongsong Luo[a,b *]

We report a novel, low-cost strategy to synthesize copper oxide (CuO) nanostructures as the high-performance supercapacitor electrodes using an alkaline solution oxidation method. The structure, morphological features, surface area and pore size distribution of the products are tuned using different types of surfactants. The CuO electrode obtained from sodium dodecyl sulfate (SDS) presents the best electrochemical performance due to the synergies arising from the large surface area and pore volume created by the ultrathin nanoleaves constituting the flower-shape nanostructure. The electrode delivers a remarkable specific capacitance of 520 F g^{-1} at 1 A g^{-1} and a high rate capacitance of 405 F g^{-1} at 60 A g^{-1} with more than 95% of Coulombic efficiency after 3500 cycles.

1. Introduction

Clean and renewable energy storage plays a key role in the development of modern electronic products, transportation, medical devices and so on.[1] Supercapacitors can offer higher power densities with longer cyclic lifespan than batteries, and store higher energies than conventional capacitors,[2-6] thus have been considered one of the most promising next generation energy-storage devices. In general, they can be divided into two categories depending on the charge storage mechanism: electric double-layer capacitors (EDLCs) and pseudo-capacitors.[7-10] EDLCs store electrical energy by accumulation of pure electrostatic charges in the electric double layer formed at the electrode-electrolyte interface, whereas pseudocapacitors rely on reversible Faradaic redox reactions that occur at the electrode surface, achieving much higher specific capacitances (SCs) than EDLCs. [8,11]

Recently, much effort has been devoted to exploring transition-metal oxides (TMOs) including RuO_2,[12] MnO_2,[13] $NiCo_2O_4$,[14] and NiO[15] because their higher SCs than carbonaceous materials and better cyclic stability than conducting polymers.[16-18] However, experimental SC values are often much lower than the theoretical predictions, because only limited external surface of the electrodes takes part in the electrochemical reactions while the electrode internal region could barely contribute to the capacitive performance.[19,20] It follows that a large specific surface area is one of the most important criteria of TMO electrode materials which enables efficient redox reactions through a large electrode-electrolyte interface, so as to maintain a large capacity by pseudocapacitors.

As an important low-cost TMO with a narrow band gap of ~1.2 eV, copper oxide (CuO) has been extensively exploited for widespread applications in sensors, lithium-ion batteries, photocatalysts, solar cell devices, and so on.[21-24] Among these potential applications, CuO has been considered a very promising candidate to replace commercial RuO_2-based pseudocapacitive materials due to its low-cost, abundance and non-toxicity. More importantly, CuO can deliver a high theoretical pseudocapacitance of ~1800 F g^{-1}, which is close to that of the widely studied $RuO_2 \cdot nH_2O$ (~ 2200 F g^{-1}).[25] Significant research efforts have been directed towards the design and development of CuO as a supercapacitor electrode, Table 1 gives a brief summary of recent developments.[26-30] Several different CuO nanostructures have been obtained using various strategies, including anodization, solvothermal growth, wet-chemical process, water bath method and potentio-dynamic electrodeposition. For example, CuO nanosheet arrays were electrochemically synthesized by anodization of a piece of copper foam in KOH aqueous solution.[26] CuO nanobelts were synthesized using a solvothermal growth method,[27] whereas cauliflower-like CuO was grown directly on a stainless steel substrate by potentio-dynamic mode of electrodeposition.[30] These methods often require high temperatures, high pressures, sophisticated instrumentation and complicated experimental procedures, so that their mass production and the application of these CuO nanostructures remain a big challenge.

With the above difficulties in mind, we have developed a facile, high-efficiency and low-cost synthetic route to prepare novel CuO nanostructures. Herein, we present an oxidation method in alkaline solution for large-scale fabrication of porous CuO nanostructures along with their growth mechanisms. The nature of crystalline structure, their shapes and pore size distributions are tuned using different surfactants and by controlling the reaction time. A strong dependence of specific charge storage capacities on the morphology and structure of CuO electrodes is demonstrated. The pseudocapacitor electrodes made from flower-shaped CuO deliver the best electrochemical performance

including the highest SCs among three different nanostructures.

2. Experimental

2.1 Materials preparation

All the reagents were of analytical grade and used without further purification. In a typical process, 6.0 cm × 3.0 cm rectangular Cu foils of 0.5 mm in thickness and 99.9% purity (Alfa Aesar) were washed in a 3 M HCl aqueous solution for 15 min to remove the surface impurities and oxide layers. To synthesize different CuO nanostructures on Cu foils, three different etchants were prepared containing two different surfactants: namely, (i) 0.8 g sodium dodecyl sulfate (SDS) (0.07 M); (ii) 0.12 g polyvinyl alcohol (PVA) (0.07 M); and (iii) without surfactant. The starting solution was prepared by mixing 4.80 g of NaOH in 40 mL of water while stirring. When the solution was cooled to room temperature, 1.37 g of $(NH_4)_2S_2O_8$ was added to the NaOH aqueous solution, and the above surfactant was introduced into the mixture. When the surfactant was completely dissolved in NaOH solution, the mixture was quickly transferred into a 50 mL of Teflon-lined stainless steel autoclave. Then, the cleaned Cu foil was immersed in the solution. The autoclaves were sealed and maintained at 80 °C for 2 h. After the reactions, the black CuO precipitates were separated from the solution by centrifugation, washed several times with ethanol and distilled water to remove any ionic residues, followed by drying in an oven at 60 °C for 10 h for characterization. Different CuO nanostructures were formed depending on the types of surfactant used: CuO flowers and CuO spheres were obtained from the solutions containing the surfactants, SDS and PVA, respectively, whereas CuO corals were synthesized without adding a surfactant.

2.2 Characterization

Thermogravimetric and differential thermal analyses (TG-DTA, SDT 2960) were conducted at a heating rate of 10 °C min^{-1} in a nitrogen atmosphere. The phase structure of the materials was characterized by X-ray diffraction (XRD) analysis on a D8 Focus (Bruker, Germany) automated X-ray diffractometer system with Cu-Kα radiation (λ=1.5418 Å). The Raman scattering measurement was carried out on a laser Raman spectrometer (Renishaw, England) at room temperature. The elemental chemistry of the materials was studied by X-ray photoelectron spectroscopy (XPS) using an AlKα X-ray source operated at 90 W (Kratos Axis Ultra DLD). Their morphologies and microstructures were characterized by field emission scanning electron microscopy (FESEM, JEOL S-4800) and transmission electron microscopy (TEM, JEOL JEM-2010). Nitrogen adsorption and desorption isotherms were determined by nitrogen physisorption at 77 K on a Micrometritics ASAP 2020 analyzer. The pore size distributions (PSDs) were calculated based on a Barrett-Joyner-Halenda (BJH) method using the nitrogen adsorption data and assuming a slit pore model.

2.3 Electrochemical measurements

The pseudocapacitive performance of the electrodes made from the CuO nanostructures were investigated on an electrochemical workstation, CHI660E (Chenhua, P. R. China) using a three-electrode system. The working electrode was prepared by mixing the active material, carbon black and polyvinylidene fluoride (PVDF) binder (10% solution in N-methyl-2-pyrollidone) with a mass ratio of 75:20:5. A 5% solution of the mixture in isopropanol was sprayed on Ni foam as the current collector. The prepared electrode was dried at 60 °C overnight. A Pt plate was used as the auxiliary electrode and Ag/AgCl as the reference electrode, with 1 M KOH solution as the electrolyte at room temperature. Cyclic voltammetry (CV) analysis was performed between 0 and 0.6 V *vs.* Ag/AgCl at scan rates ranging from 5 to 100 mV s^{-1}. Galvanostatic charge/discharge test was conducted in a stable potential window at different current densities of 1-60 A g^{-1}. Electrochemical impedance spectroscopy (EIS) was performed at an AC voltage of 5 mV in the frequency range from 0.01 Hz to 100 kHz. The

Table 1 Summary of CuO-based supercapacitors with their key performance characteristics.

Method of synthesis	Morphology	C_s (F g^{-1})	Discharge current density	Electrolyte	Stability	Ref.
Electrospun	Nanowire	620	5 mA cm^{-2}	6 M KOH	10% loss after 2000 cycles	25
Anodization	Nanosheet	212	0.41 mA mg^{-1}	6 M KOH	15% loss after 850 cycles	26
Solvothermal method	Nanobelt	392	2 A g^{-1}	1 M KOH	10-15% loss after 5000 cycles	27
Wet-chemical process	Gear-like nanostructure	348	1 A g^{-1}	0.1 M KOH	12.1% loss after 2000 cycles	28
Water bath method	Nanoflower	130	1 A g^{-1}	6 M KOH	29.8% loss after 7000 cycles	29
Potentiodynamic Electrodeposition	Cauliflower-like nanostructure	162	2 mA cm^{-1}	1 M Na$_2$SO$_4$	19% loss after 2000 cycles	30
Alkaline solution oxidation method	Nanoflower	520	1 A g^{-1}	1 M KOH	5.5% loss after 5000 cycles	This work
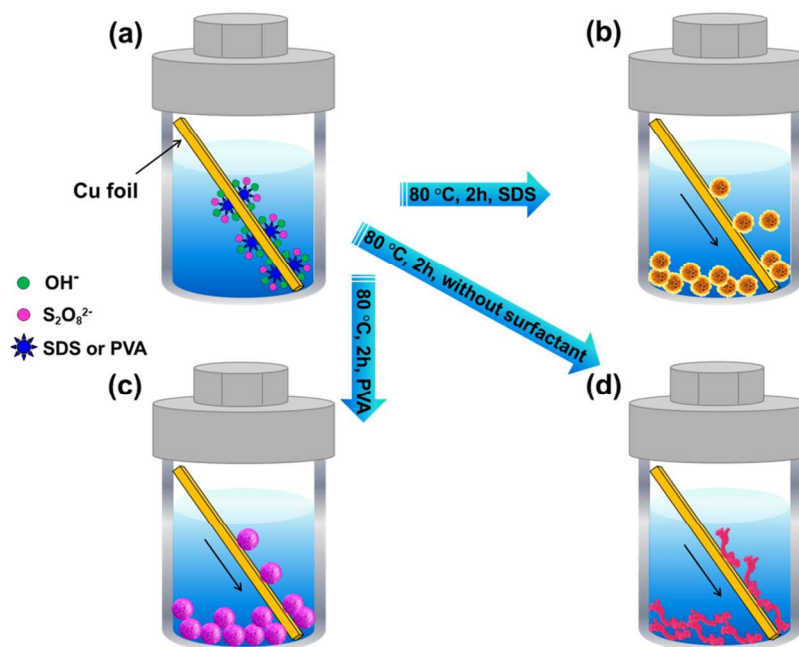
Fig. 1 Schematics illustrating the fabrication processes of CuO nanostructures with three different morphologies: (a) functionalization of CuO nanomaterials in solution; (b) CuO flowers; (c) CuO spheres; and (d) CuO corals.

nominal area of the CuO/Ni foam electrode immersed in the electrolyte was controlled at around 1 cm × 1 cm. The loading mass of the active materials was ~5 mg cm^{-2}. The SCs of the CuO/Ni foam electrodes were estimated from the cathodic or anodic part of the CV curves according to the following equation:
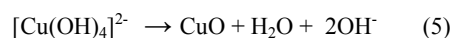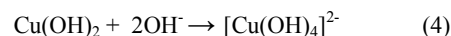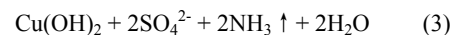
$$C_s = \frac{\int I dV}{v \Delta V m} \qquad (1)$$
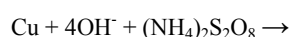
where I (A) is the response current, v (V s^{-1}) is the potential scan rate, ΔV (V) is the potential window, and m (g) is the mass of the active electrode material. Also, the SCs of the CuO/Ni foam electrodes were calculated from the galvanostatic discharge curves according to the following equation:

$$C_s = I \Delta t / \Delta V m \qquad (2)$$

where C_s, I, Δt, ΔV and m are the specific capacitance, the constant discharge current, the total discharge time, the potential window and the mass of the electroactive materials, respectively.

3. Results and discussion

The alkaline solution oxidation process and the resulting CuO nanostructures are schematically illustrated in Fig. 1. A Cu foil was immersed in an alkali solution, where it was oxidized and dissolved by OH$^-$ and $S_2O_8^{2-}$ ions, and Cu^{2+} ions were eluted from the substrate (Fig. 1a). With the lapse of time, oxidation of Cu foil and eventual dehydration yielded black CuO precipitates. SDS or PVA did not directly take part in the reaction, but rather acted as a structure directing agent. The whole synthetic process involved the following chemical reactions:

$$Cu + 4OH^- + (NH_4)_2S_2O_8 \rightarrow$$

$$Cu(OH)_2 + 2SO_4^{2-} + 2NH_3 \uparrow + 2H_2O \qquad (3)$$

$$Cu(OH)_2 + 2OH^- \rightarrow [Cu(OH)_4]^{2-} \qquad (4)$$

$$[Cu(OH)_4]^{2-} \rightarrow CuO + H_2O + 2OH^- \qquad (5)$$

Under different reaction conditions, different nanostructures were synthesized, namely CuO flowers, CuO spheres and CuO corals (Fig. 1b-d).

The XRD spectrum of the CuO flowers is shown in Fig. 2a. All the diffraction peaks are indexed according to the standard monoclinic structure of CuO crystal (JCPDS file No. 45-0937). No peaks of impurities, such as copper hydroxide or cuprous oxides,
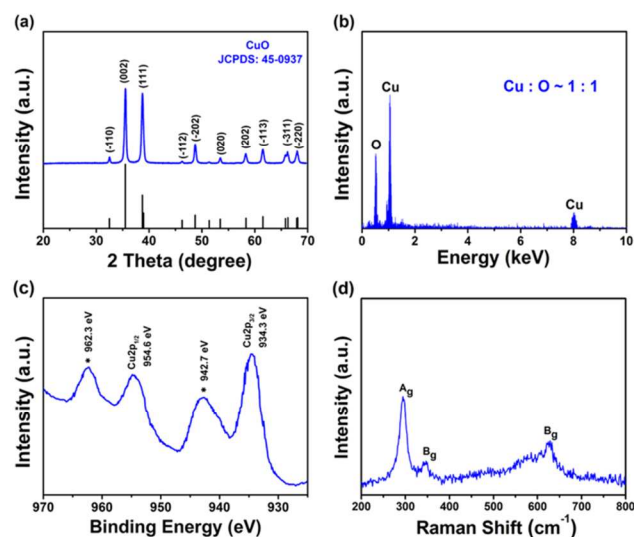
Fig. 2 XRD pattern (a), EDX spectrum (b), Cu 2p core-level XPS spectrum (c), and Raman spectrum (d) of CuO flowers.
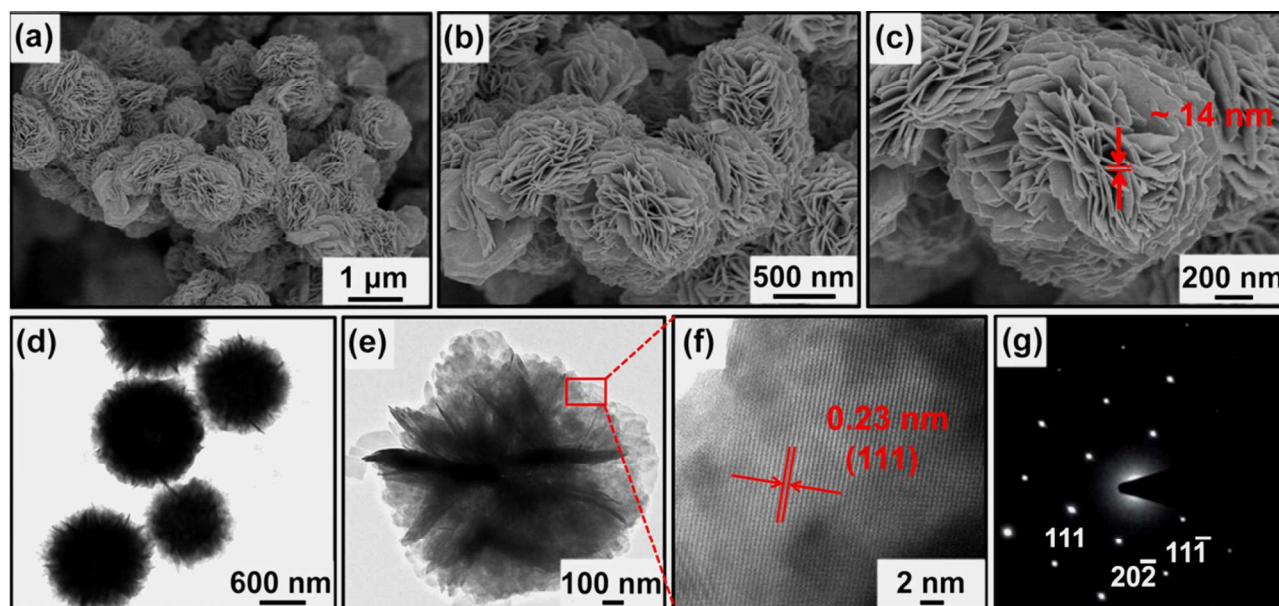
ARTICLE TYPE

Fig. 3 (a, b, c) SEM images; (d, e) TEM images of CuO flowers taken at different magnifications; (f) HRTEM image of the fringe part of flower, and (g) the corresponding SAED result.

were found, suggesting high purity of the material. The EDX analysis
5 showed only copper and oxygen (see Fig. 2b), confirming the XRD
result. Further evidence of the composition and purity of the material
was obtained by XPS of the core-level Cu 2p, as shown in Fig. 2c.
The peaks at 954.1 and 934.1 eV correspond to the core-level Cu
$2p_{1/2}$ and Cu $2p_{3/2}$ transitions of copper, respectively.[31] Moreover, the
10 presence of satellite peaks (with asterisks in Fig. 2c) at higher binding
energy sides, whose intensities are comparable to those of the core-
level Cu 2p peaks, further demonstrates that the flower-like structure
consisted of pure CuO crystals.[32] Additional information was
obtained by Raman spectroscopy in the range of 200-800 cm^{-1}, as
15 shown in Fig. 2d. The broad peak with a relatively high intensity at
295 cm^{-1} is assigned to A_g band, while the two peaks at 342.8 and
628.5 cm^{-1} are assigned to $2B_g$. The significant intensities of these
peaks indicate a single phase and high crystallinity of CuO flowers,
in good agreement with the previous reports.[33,34] The
20 thermogravimetric analysis shows that there was a very small weight
loss, ~2 wt.%, below 200 ^{o}C, which can be attributed to the
evaporation of adsorbed moisture (Fig. S1). There was virtually no
weight loss between 200 and 600 ^{o}C, indicating the absence of ionic
liquids in the material. This further confirms the high purity of the as-
25 prepared CuO flowers.

The morphologies and structures of CuO flowers were
examined by SEM and TEM. Fig. 3a-c clearly present flower-like
CuO crystals with a high yield, mostly within the size distribution
ranging 1.2-1.8 μm and with an average of 1.5 μm (Fig. S2). The
30 single flower was composed of many nano-sized leaves of 10-20
nm in thickness arising from the flower center. The TEM images
(Fig. 3d, e) suggest that the flower core was densely filled with
leaves whereas the flower edge had a porous structure due to the

gaps between the flower leaves. The lattice fringe spacing of
35 0.23 nm marked in Fig. 3f corresponds to the (111) plane of
monoclinic CuO. The selected area electron diffraction (SAED)
pattern (Fig. 3g) can be indexed to a pure monoclinic phase. The
appearance of periodic diffraction spots indicates that these
nanostructures were self-assembled into highly oriented
40 aggregates and diffracted as a single crystal.

CuO corals and spheres were prepared using a different
surfactant or without surfactant, and Fig. 4 shows their
morphologies. The corals had an average length of 2.7 μm,
approximate widths of 200-450 nm, and thicknesses of 300-550 nm
45 (Fig. 4a, c). The simpler geometry and the elongated shape may
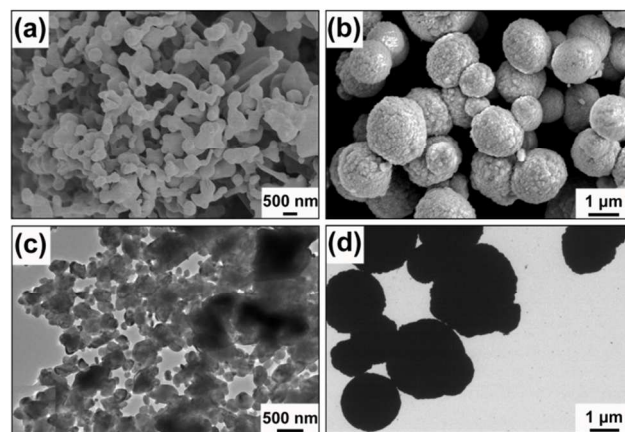imply that the absence of surfactant led to faster growth along the

Fig. 4 SEM and TEM images of CuO corals (a, c) and CuO spheres (b, d).

RSC Advances Accepted Manuscript

length of nanostructures, relative to the growth into the other geometries. Meanwhile, spherical particles of 0.8-1.5 μm in diameter with a relatively clean surface were created when the PVA surfactant was added into the reaction solution (Fig. 4b, d).
5 When PVA was used as a template, the aqueous solution of Cu^{2+} and PVA led to the formation of nucleation seeds to act as an initial nucleus for the growth of particles. When the particle reached a critical dimension, PVA was adsorbed onto the small particles through -OH bonds to serve as a template for the
10 formation of spheres. The rough surface of the solid CuO spheres indicates that they consisted of many primary nanoparticles.

The largely different morphologies due to the use of different types of surfactants need further explanations. It is well known that the surfactant in a solution aggregates into micelles when its
15 concentration exceeds a critical micelle concentration (CMC). Depending on the concentration and surrounding medium of the surfactant, the micelles display different shapes (Fig. 5). During the reaction in the presence of SDS, $Cu(OH)^{4-}$ could be dissociated to Cu^{2+} and OH^-, and SDS coordinates with Cu^{2+} to
20 form $Cu(SDS)_2$. In the subsequent reaction, $Cu(SDS)_2$ acts as surfactant. The concentration of 0.07 M SDS in water is considered above the CMC, so that micelles are organized in the system where the micelles play the role of "seeds"[35] to form CuO clusters on them which further grow to become 3D hierarchical
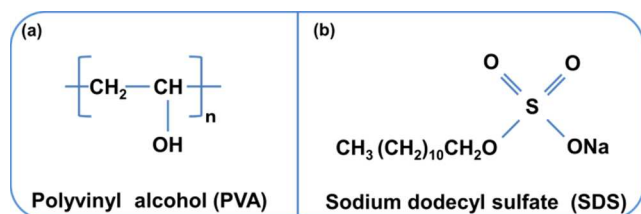25 flowers.

Fig. 5 Chemical structures of (a) polyvinyl alcohol (PVA) and (b) sodium dodecyl sulfate (SDS).

To determine the porosity of CuO nanostructures, N_2 adsorption-
30 desorption isothermal analyses were performed. According to the IUPAC classification of hysteresis loops,[36] Fig. 6a displays the type IV isotherms with type H_3 hysteresis loops. All three nanostructures did not exhibit limited adsorption at relative pressures from 0 to 1, proving the presence of typical hierarchical
35 porosities.[37,38] An increase in slope at about 0.4, especially for CuO flowers, corresponds to capillary condensation, typical of mesoporous materials, while a further increase in adsorbed volume at higher relative pressures indicates inter-particle porosity.[39] The specific surface areas of the nanostructures
40 calculated by the Brunauer-Emmett-Teller (BET) model are given in Table 2, showing increasingly larger surface areas and pore volumes in the ascending order of spheres, corals and flowers. The pore size distribution shown in Fig. 6b indicates that both the flowers and corals had both small (< 10 nm) and large
45 mesopores (> 10 nm). On the contrary, the spheres showed only small mesopores (~ 4.75 nm). In view of the dependence of pore size distributions on nanostructures, it can be summarized that the structural evolution is an important factor influencing the interconnected pores inside the particles and the void spaces between
50 them.[40]

Table 2 Surface areas and impedance parameters calculated from the equivalent circuit of the three electrodes.

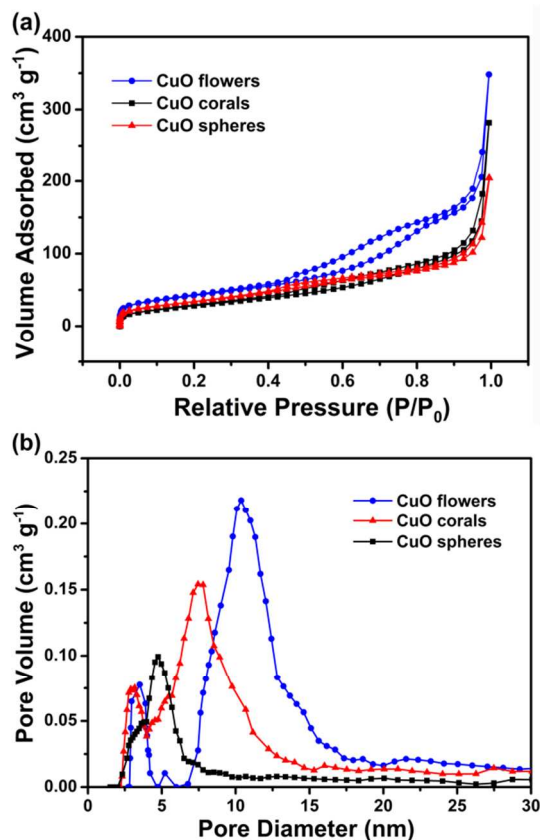| Electrodes	Surface area / $m^2 g^{-1}$	Pore volume / $cm^3 g^{-1}$	R_s / Ω	R_{ct} /Ω
CuO flowers	119.6	0.413	0.94	0.54
CuO corals	73.5	0.351	0.99	1.17
CuO spheres	36.1	0.233	1.31	5.94

55 **Fig. 6** (a) Nitrogen adsorption and desorption isotherms measured at 77 K for CuO nanostructures; and (b) corresponding Barrett-Joyner-Halenda (BJH) pore size distribution curves.

The performance of these CuO nanostructures as supercapacitor electrodes was characterized by cyclic voltammetry (CV) measurements
60 in KOH aqueous solution at room temperature (Fig. 7). All the CV curves showed a pair of redox peaks, very much different from that of an EDLC, which is normally in the form of an ideal rectangle. The well-defined redox peaks in the potential range of 0-0.6 V arose mainly from the reversible Faradaic redox
65 reactions of Cu^+ and Cu^{2+} species associated with the OH^- ions.[41] In addition, as the scan rate increased from 5 to 100 mV s^{-1}, the current density increased while the CV curve shapes changed little. Especially for CuO flower electrode, the anodic peak potential at about 0.56 V shifted towards the anodic direction
70 whereas the cathodic peak potential at about 0.22 V shifted towards the cathodic direction. Compared with the CuO coral and
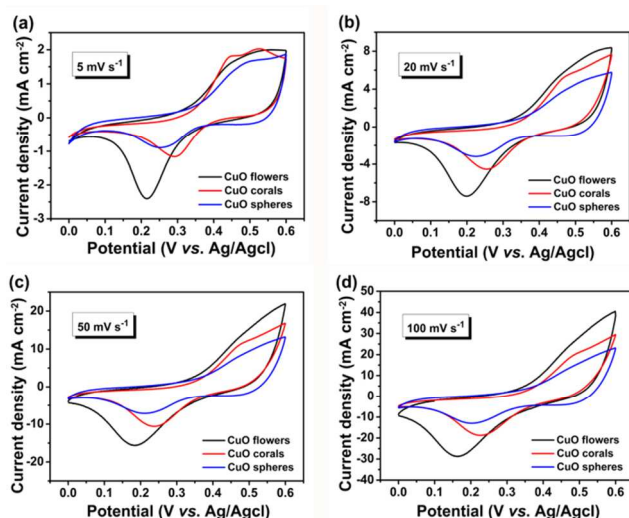
Fig. 7 Cyclic voltammetry (CV) curves of CuO nanostructures in 1 M KOH aqueous solution over a potential range from 0 to 0.6 V at a scan rate of (a) 5, (b) 20, (c) 50 and (d) 100 mV s^{-1}.

sphere counterparts, the CuO flower electrode maintained distinct redox peaks at high scan rates (Figs. 7 and S3a, b). This observation might be due to the bigger size pores in flowers than the other nanostructures, which promoted ion diffusion. The electrode made from CuO flowers exhibited the highest current density (Fig. 7) making them most promising for pseudocapacitor electrodes among the three nanostructures. The smaller active specific surface areas and pore volumes of the CuO coral and sphere electrodes presented inferior cyclic voltammetry performance.

Fig. 8a shows a Nyquist plot of CuO-based electrode materials measured in 1 M KOH in the frequency range from 0.01 Hz to 100 kHz. The intercept at the real part of high frequency represents the combination (R_s) of ionic resistance of electrolyte, intrinsic resistance of substrate and contact resistance at the active material/current collector interface.[42] The charge transfer resistance (R_{ct}) is caused by the Faradic reactions and the double-layer capacitance on the grain surface.[43] The electrical equivalent circuit used for fitting the impedance spectra is shown in the inset of Fig. 8a, and Table 2 presents these parameters fitted by Zview software. Both the R_s and R_{ct} values of the CuO flower electrode were lower than those of the corals and spheres. At low frequencies, the flower electrode had a linear line with a steeper slope and shorter length than the other nanostructures, indicating a lower Warburg impedance (Z_w) encountered during the ion transportation in the aqueous electrolyte. Moreover, ion diffusion coefficient of all the morphologies is calculated according to the following equation[44]:

$$D = R^2 T^2 / 2A^2 n^4 F^4 C^2 \sigma^2 \qquad (6)$$

where the meanings of n is the number of electrons per molecule during oxidization, A is the geometric surface area of the electrode, D is the diffusion coefficient of OH$^-$ ion, R is the gas constant, T is the absolute temperature, F is the Faraday constant, C is the concentration of OH$^-$ ion, and σ is the Warburg factor which has relationship with Z_{re}:

$$Z_w = R_s + R_{ct} + \sigma\omega^{-1/2} \qquad (7)$$

where the meaning of $\omega^{-1/2}$ is the square root of frequency in the low-frequency region. According to Eqs. (6) and (7), the ion diffusion coefficients of flowers, croals and spheres are calculated to be 15.3×10^{-10}, 12×10^{-10} and 1.7×10^{-10} cm^2 s^{-1}, respectively. The improved EIS performance of the flower electrode is related to the large specific surface area and the excellent porosity characteristics arising from the flower-shaped nanoparticles consisting of numerous nanoleaves, offering transport channels and reducing the electron/ion diffusion paths.

Fig. 8b shows a summary of the CV curves of the flower electrode taken from Fig. 7 with a typical pseudocapacitive behaviour and distinct redox peaks even at a high potential scan rate of 100 mV s^{-1}. Similar CV curves for the other electrode materials are given in Fig. S3a, b. Fig. S4 investigates the relationship between the SC$_s$ of the flower electrode or capacity retention and scan rate, exposing excellent specific capacitance of 615, 595, 563, 549, 525, and 500 F g^{-1} at scan rates of 5, 10, 20, 30, 50 and 100 mV s^{-1}, respectively. This shows that about 81.3% of the capacitance is still retained when the scan rate increased from 5 to 100 mV s^{-1}. In pseudocapacitive materials, we can conclude from the scan rate (v) dependence of voltammetric current (I) that the capacitance originates from surface redox reactions or from bulk diffusion.[25] That is to say, the $I \propto v$ for surface redox reactions and $I \propto \sqrt{v}$ for semi-infinite bulk diffusion.[45] In the case of CuO flower, the relationship between peak current and scan rate is plotted in Fig. S5a, the peak current varied linearly with scan rate. As far as we know, ion movement is limited only to the surfaces of the electrode material at higher voltammetric scan rates (> 30 mV s^{-1}). Therefore, the high SC$_s$ of flower electrode resulted from surface redox reaction, and remained practically constant with scan rate. Meanwhile, we also surveyed the other two electrodes (Fig. S5b, c). From both the linear relationship between peak current and scan rate as well as the symmetry of anodic/cathodic peak, CuO flower electrode exhibits prominent electrochemical reversibility.

The SCs of the electrode materials were measured in the voltage range of 0-0.6 V (vs. Ag/AgCl). Typical galvanostatic discharge profiles of the three electrodes measured at different current densities are shown in Figs. 8c and S3c, d. The potential drop in the discharge curves is generally caused by internal resistance and incomplete Faradic reactions in the electrode.[39] The SCs of the electrodes calculated according to Eq (1) are plotted as a function of current density, as shown in Fig. 8d. The flower electrode delivered the highest SCs among the three at all current densities studied: e.g. 520 and 405 F g^{-1} at 1 and 60 A g^{-1}, respectively. These values are at least 30% higher than those of the coral electrode or 50% higher than those of the sphere electrode at the same discharge current densities.

High rate capability and long cyclic life are among the vital indicators for practical application of a pseudocapacitor. The CuO flower electrode was subjected to continuous charging and discharging for 5000 cycles at increasingly higher current densities, as shown in Fig. 9a. The SC progressively increased in the first 500 cycles at 1 A g^{-1} before reaching a maximum of 529 F g^{-1}, as a result of the gradual activation of the electrode material. It is worth noting that even after 3000 cycles, the electrode retained a remarkable SC of 405 F g^{-1} at a high current density of 60 A g^{-1} while it showed 495 F g^{-1} after the current
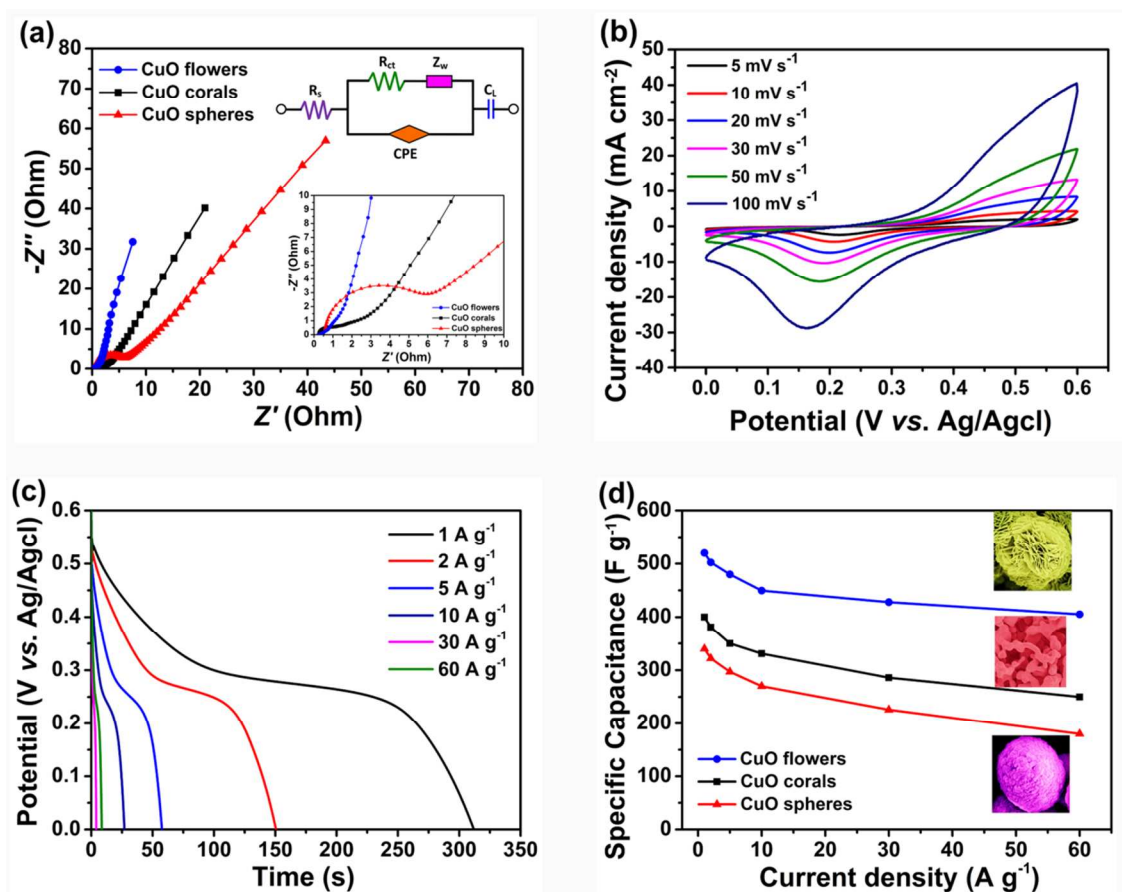
Journal Name

ARTICLE TYPE

Fig. 8 (a) Electrochemical impedance spectra (EIS) obtained from the CuO-based electrodes (inset: the corresponding equivalent circuit); (b) cyclic voltammograms of CuO flower electrode at different scan rates; (c) typical galvanostatic discharge profiles of CuO flowers electrode at different current densities; (d) specific capacitances of three different CuO nanostructured electrodes as a functional of current density.
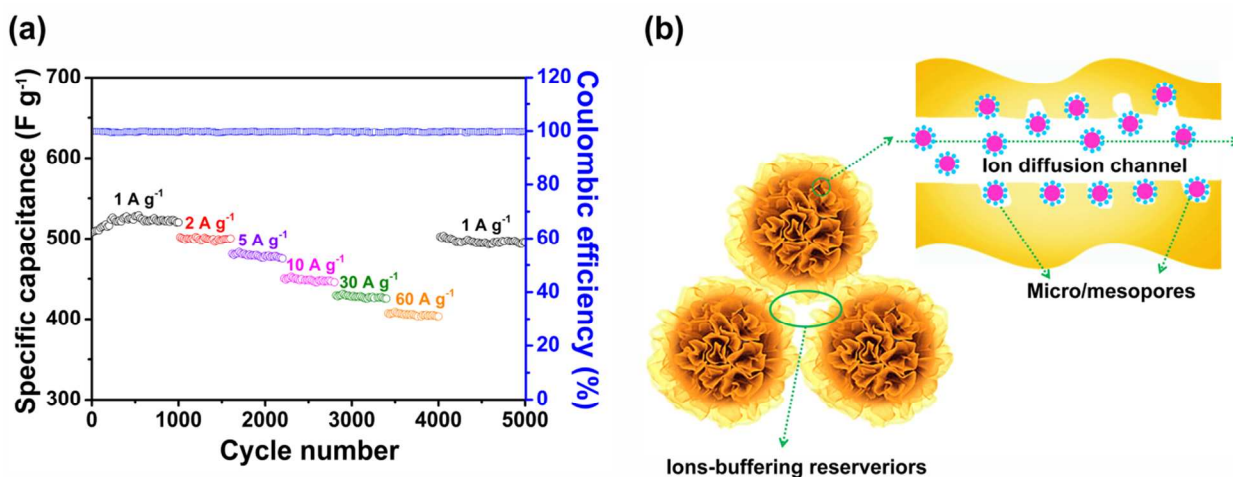
5

Fig. 9 (a) Cycling performance and Coulombic efficiency of the CuO flower electrode at progressively higher current densities; (b) schematic of the hierarchical porous structure.

ARTICLE TYPE

density was returned to 1 A g^{-1}. During all these charge/discharge cycles at different rates, the Coulombic efficiency was steadily kept higher than 99 %, confirming exceptional cyclic stability. Several synergies arising from the unique morphological features and the hierarchical pore structure of the CuO flowers gave rise to such remarkable electrochemical performance. As the basis of the flower-shaped structure, the well-separated primary nanoleaves were exposed to the electrolyte solution, to the benefit of fast electron/ion transfer. The hierarchical porous architecture greatly increased the surface area, offering sufficient diffusion channels, facilitating the electrolyte to diffuse more easily into the inner region of the electrode (Fig. 9b). In addition, the sufficient void spaces between the neighbouring nanoleaves, owing to their role of ion buffering reservoirs, ensured sufficient redox reactions to take place at high current densities.

4. Conclusions

In summary, hierarchical porous CuO flowers were successfully synthesized using a rapid and facile alkaline solution oxidation process. Addition of organic surfactants changes the morphology, surface area and pore size distribution of CuO nanostructures which consequently affected the electrochemical properties of the CuO electrodes. The highly porous CuO flowers with a very large surface area offered many advantages for supercapacitor applications. They delivered ultrahigh SCs of 520 and 405 F g^{-1} at current densities of 1 and 60 A g^{-1}, respectively. Even after 5000 cycles at various high current densities, a capacitance of 495 F g^{-1} at 1 A g^{-1} with 95.2 % retention was achieved. In addition to the remarkable electrochemical performance, the 3D hierarchical CuO flowers electrode had other advantages, including low cost, simple synthesis routes and high reproducibility.

Acknowledgements

Notes and references

aSchool of Physics and Electronic Engineering, Xinyang Normal University, Xinyang 464000, P. R. China. E-mail: ysluo@xynu.edu.cn
bKey Laboratory of Advanced Micro/Nano Functional Materials, Xinyang Normal University, Xinyang 464000, P. R. China.
cSchool of Material Science and Engineering, Hebei University of Technology, Tianjin 300130, P. R. China. E-mail: tangcc@hebut.edu.cn
dCollege of Chemistry and Chemical Engineering, Luoyang Normal University, Luoyang 471022, P. R. China.
eDepartment of Mechanical and Aerospace Engineering, The Hong Kong University of Science and Technology, Clear Water Bay, Kowloon, Hong Kong, P. R. China.

† Electronic Supplementary Information (ESI) available: TG-DTA curves, size distribution of CuO flowers, and Electrochemical characterization of the CuO flowers, corals and spheres.

1 S. Yuan, X. L. Huang, D. L. Ma, H. G. Wang, F. Z. Meng and X. B. Zhang, *Adv. Mater.*, 2014, **26**, 2273.
2 Z. Li, Z. W. Xu, H. L. Wang, J. Ding, B. Zahiri, C. M. B. Holt, X. H. Tan and D. Mitlin, *Energy Environ. Sci.*, 2014, **7**, 1708.
3 M. J. Deng, P. J. Ho, C. Z. Song, S. A. Chen, J. F. Lee, J. M. Chen and K. T. Lu, *Energy Environ. Sci.*, 2013, **6**, 2178.
4 X. H. Lu, G. M. Wang, T. Zhai, M. H. Yu, J. Y. Gan, Y. X. Tong and Y. Li, *Nano Lett.*, 2012, **12**, 1690.
5 H. L. Wang, Q. M. Gao and L. Jiang, *Small*, 2011, **7**, 2454.
6 P. Simon and Y. Gogotsi, *Nat. Mater.*, 2008, **7**, 845.
7 B. Wang, T. Zhu, H. B. Wu, R. Xu, J. S. Chen, and X. W. Lou, *Nanoscale*, 2012, **4**, 2145.
8 Q. F. Wang, X. F. Wang, B. Liu, G. Yu, X. J. Hou, D. Chen and G. Z. Sheng, *J. Mater. Chem. A*, 2013, **1**, 2468.
9 Z. Chen, Y. C. Qin, D. Weng, Q. F. Xiao, Y. T. Peng, X. L. Wang, H. X. Li, F. Wei and Y. F. Lu, *Adv. Funct. Mater.*, 2009, **19**, 3420.
10 J. W. Xiao and S. H. Yang, *RSC Advances*, 2011, **1**, 588.
11 L. Huang, D. C. Chen, Y. Ding, S. Feng, Z. L. Wang and M. L. Lin, *Nano Lett*, 2013, **13**, 3135.
12 C. C. Hu, K. H. Chang, M. C. Lin and Y. T. Wu, *Nano Lett.*, 2006, **6**, 2690.
13 Y. S. Luo, J. Jiang, W. W. Zhou, H. P. Yang, J. S. Luo, X. Y. Qi, H. Zhang, D. Y. W. Yu, C. M. Li, and T. Yu, *J. Mater. Chem.*, 2012, **22**, 8634.
14 C. Z. Yuan, J. Y. Li, L. R. Hou, X. G. Zhang, L. F. Shen and X. W. Lou, *Adv. Funct. Mater.*, 2012, **22**, 4592.
15 S. Vijayakumar, S. Nagamuthu and G. Muralidharan, *ACS Appl. Mater. Interfaces*, 2013, **5**, 2188.
16 X. Y. Liu, Y. Q. Zhang, X. H. Xia, S. J. Shi, Y. Lu, X. L. Wang, C. D. Gu and J. P. Tu, *J. Power Sources*, 2013, **239**, 157.
17 W. Sugimoto, H. Iwata, Y. Yasunaga, Y. Murakami and Y. Takasu, *Angew. Chem.*, *Int. Ed.*, 2003, **42**, 4092.
18 M. Hughes, G. Z. Chen, M. S. P. Shaffer, D. J. Fray and A. H. Windle, *Chem. Mater.*, 2002, **14**, 1610.
19 Y. G. Li, P. Hasin and Y. Y. Wu, *Adv. Mater.*, 2010, **22**, 1926.
20 L. Yu, G. Q. Zhang, C. Z. Yuan and X. W. Lou, *Chem. Commun.*, 2013, **49**, 137.
21 S. Sahoo, S. Husale, B. Colwill, T. M. Lu, S. Nayak and P. M. Ajayan, *ACS Nano*, 2009, **3**, 3935.
22 J. C. Park, J. Kim, H. Kwon and H. Song, *Adv. Mater.*, 2009, **21**, 803.
23 Q. Yu, H. W. Huang, R. Chen, P. Wang, H. S. Yang, M. X. Gao, X. S. Peng and Z. Z. Ye, *Nanoscale*, 2012, **4**, 2613.
24 Y. L. Liu, L. Liao, J. C. Li and C. X. Pan, *J. Phys. Chem. C*, 2007, **111**, 5050.
25 B. Vidhyadharan, I. I. Misnon, R. A. Aziz, K. P. Padmasree, M. M. Yusoff and R. Jose, *J. Mater. Chem. A*, 2014, **2**, 6578.
26 Y. H. Li, S. Chang, X. L. Liu, J. C. Huang, J. L. Yin, G. L. Wang and D. X. Cao, *Electrochim. Acta*, 2012, **85**, 393.
27 X. J. Zhang, L. T. Yu, L. L. Wang, R. Ji, G. F. Wang and B. Y. Geng, *Phys. Chem. Chem. Phys.*, 2013, **15**, 521.
28 L. T. Yu, Y. Y. Jin, L. L. Li, J. Ma, G. F. Wang, B. Y. Geng and X. J. Zhang, *CrystEngComm*, 2013, **15**, 7657.
29 B. J. Heng, C. Qing, D. M. Sun, B. X. Wang, H. Wang and Y. W. Tang, *RSC Adv.* 2013, **3**, 15719.
30 D. P. Dubal, G. S. Gund, C. D. Lokhande and R. Holze, *Mater. Res. Bull.*, 2013, **48**, 923.
31 S. D. Sun, X. Z. Zhang, Y. X. Sun, S. C. Yang, X. P. Song and Z. M. Yang, *ACS Appl. Mater. Interfaces*, 2013, **5**, 4429.
32 D. Q. Gao, G. J. Yang, J. Y. Li, J. Zhang, J. L. Zhang and D. S. Xue, *J. Phys. Chem. C*, 2010, **114**, 18347.

RSC Advances Accepted Manuscript

33 M. A. Dar, Q. Ahsanulhaq, Y. S. Kim, J. M. Sohn, W. B. Kim and H. S. Shin, *Appl. Surf. Sci.*, 2009, **255**, 6279.

34 X. Wang, G. Xi, S. Xiong, Y. Liu, B. Xi, W. Yu, Y. Qian, *Cryst. Growth Des.*, 2007, **7**, 930.

5 35 Y. Liu, Y. Chu, M. Y. Li, L. L. Li and L. H. Dong, *J. Mater. Chem.*, 2006, **16**, 192.

36 W. Xiong, M. X. Liu, L. H. Gan, Y. K. Lv, Y. Li, L. Yang, Z. J. Xu, Z. X. Hao, H. L. Liu and L. W. Chen, *J. Power Sources*, 2011, **196**, 10461.

10 37 D. Grosso, G. Illia, E. L. Crepaldi, B. Charleux and C. Sanchez, *Adv. Funct. Mater.*, 2003, **13**, 37.

38 J. R. Matos, M. Kruk, L. P. Mercuri, M. Jaroniec, L. Zhao, T. Kamiyama, O. Terasaki, T. J. Pinnavaia and Y. Liu, *J. Am. Chem. Soc.*, 2003, **125**, 821.

15 39 Y. Lu, K. W. Qiu, D. Y. Zhang, J. Lin, J. Y. Xu, X. M. Liu, C. C. Tang, J. K. Kim and Y. S. Luo, *RSC Adv.* 2014, **4**, 46814.

40 Y. Lu, H. L. Yan, D. Y. Zhang, K. W. Qiu, J. Lin, Y. M. Xue, J. Li, C. C. Tang and Y. S. Luo, *J. Solid State Electrochem.*, 2014, **18**, 3143.

41 G. L. Wang, J. C. Huang, S. L. Chen, Y. Y. Gao and D. X. Cao, *J. 20 Power Sources*, 2011, **196**, 5756.

42 A. Laheäär, A. Jänes and E. Lust, *Electrochim. Acta*, 2012, **82**, 309.

43 Z. Fan, J. Yan, T. Wei, L. Zhi, G. Ning, T. Li and F. Wei, *Adv. Funct. Mater.*, 2011, **21**, 2366.

44 H. Liu, C. Li, H. P. Zhang, L. J. Fu, Y. P. Wu and H. Q. Wu, *J. Power 25 Sources*, 2006, **159**, 717.

45 I. E. Rauda, V. Augustyn, B. Dunn and S. H. Tolbert, *Acc. Chem. Res.*, 2013, **46**, 1113.

30

35

40

45